Estimation of spatial distribution and fluid fraction of a potential supercritical geothermal reservoir by magnetotelluric data: a case study from Yuzawa geothermal field, NE Japan

Keiichi Ishizu[1], Yasuo Ogawa[1], Keishi Nunohara[2], Noriyoshi Tsuchiya[2], Masahiro Ichiki[3], Hideaki Hase[1,6], Wataru Kanda[1], Shinya Sakanaka[4], Yoshimori Honkura[1], Yuta Hino[1], Kaori Seki[1,7], Kuo Hsuan Tseng[1,8], Yusuke Yamaya[5], and Toru Mogi[1]

[1] Volcanic Fluid Research Center, Tokyo Institute of Technology, Tokyo, Japan

[2] Graduate School of Environmental Studies, Tohoku University, Miyagi, Japan

[3] Graduate School of Science, Tohoku University, Miyagi, Japan

[4] Graduate School of International Resource Sciences, Akita University, Akita, Japan

[5] Fukushima Renewable Energy Institute, National Institute of Advanced Industrial Science and Technology, Fukushima, Japan

[6] Now at Geothermal Energy Research & Development Co., Ltd., Tokyo, Japan

[7] Now at Groundwater and Hydrology Group, Kokusai Kogyo Co., Ltd., Tokyo, Japan

[8] Now at Sumiko Resources Exploration & Development Co., Ltd., Tokyo, Japan

Corresponding author: Keiichi Ishizu (ishizu.k.ab@m.titech.ac.jp)

Key points:

- A supercritical geothermal reservoir of 3 km (width) × 5 km (length) was imaged by the magnetotelluric method at a depth of 2.5–6 km.
- The fluid fraction of the supercritical reservoir was estimated to be 0.5–2% with a salinity of 5–10 wt%.
- Upwelling supercritical fluids supplied from the melt were trapped under a less-permeable silica sealing.

Abstract

Magmatic fluids within the crust may exist under supercritical conditions (e.g. >374°C and >22.1 MPa for pure water). Geothermal systems using such supercritical fluids have gained attention as unconventional geothermal resources because they can offer significantly more energy than conventional geothermal fluids with temperatures <350°C. Although an understanding of the spatial distribution and fluid fraction of supercritical geothermal reservoirs is necessary for their resource assessment, the spatial distribution and fluid fraction of supercritical geothermal reservoirs worldwide are poorly understood due to the limited number of geophysical observations. Here, the magnetotelluric (MT) method with electrical resistivity imaging was used

in the Yuzawa geothermal field, northeastern Japan, to obtain information on the fluid fraction and spatial distribution of a supercritical geothermal reservoir. Our MT data revealed a potential supercritical geothermal reservoir (>400°C) with a horizontal dimension of 3 km (width) × 5 km (length) at a depth of 2.5–6 km. The estimated fluid fraction of the supercritical reservoir was 0.5–2% with a salinity of 5–10 wt%. The melt was imaged below a supercritical geothermal reservoir. Based on the resistivity model, we propose a mechanism for the evolution of a supercritical fluid reservoir, wherein upwelling supercritical fluids supplied from the melt are trapped under less permeable silica sealing. As a result, supercritical fluids accumulate under the silica sealing. This study is the first to present a detailed estimation of the spatial distribution and fluid fraction of a potential supercritical geothermal reservoir.

Plain language summary

As the demand for clean, renewable energy increases worldwide, geothermal energy has emerged as a clean and renewable energy source. Subsurface fluids in a supercritical state (high temperature and pressure of >374°C and >22.1 MPa) have gained attention as next-generation geothermal resources because they can offer significantly more energy than conventional geothermal fluids with temperatures <350°C. Supercritical geothermal fluids are believed to be found in various volcanic areas worldwide. Although an understanding of the spatial distribution and fluid fraction of supercritical fluids is necessary for their resource assessment, the spatial distribution and fluid fraction of supercritical geothermal reservoirs are poorly understood. Therefore, we used the magnetotelluric (MT) method to obtain information on the spatial distribution and fluid fraction of a supercritical geothermal reservoir in the Yuzawa geothermal field, northeastern Japan. Our MT data revealed a potential supercritical geothermal reservoir of 3 km (width) × 5 km (length) at a depth of 2.5–6 km with a fluid fraction estimated to be 0.5–2% and a salinity of 5–10 wt%. This study presents the first detailed estimation of the spatial distribution and fluid fraction of a potential supercritical geothermal reservoir.

1. Introduction

Magmatic fluids with high temperatures may exist in a supercritical state (e.g. >374°C and >22.1 MPa for pure water, and >406°C and >29.8 MPa for seawater salinity) at a depth of about 2–10 km beneath volcanic areas (Bali et al., 2020; Fournier, 1999; Friðleifsson et al., 2020; Ikeuchi et al., 1998; Reinsch et al., 2017; Scott et al., 2015; Tsuchiya et al., 2016). In fact, several deep drilling expeditions have found magmatic fluid in a supercritical state. An exploration well (WD-1a) in the Kakkonda geothermal area in northeastern (NE) Japan found magmatic fluid at 500°C at a depth of 3729 m (Doi et al., 1998; Ikeuchi et al., 1998), wherein the fluid at the bottom of the well was under supercritical conditions (Saishu et al., 2014; Tsuchiya & Hirano, 2007). Similarly, an exploratory well drilled by the Iceland Deep Drilling Project (IDDP) also encountered a reservoir of supercritical fluids at a temperature of 450°C in the Krafla volcanic system (Elders et al., 2014; Scott et al., 2015).

Geothermal systems using supercritical fluids have recently gained attention as next-generation geothermal resources (Friðleifsson et al., 2020; Okamoto et al., 2019; Parisio et al., 2019; Reinsch et al., 2017; Stimac et al., 2017; Watanabe et al., 2017). Various countries, including Japan, the USA, New Zealand, and Italy, are beginning to consider the development of power

plants using supercritical fluids (Reinsch et al., 2017).. This newfound attention comes from the fact that supercritical fluids have significant advantages as a source of energy: a higher enthalpy per unit mass and a lower fluid viscosity than conventional geothermal fluids with temperatures <350°C (Reinsch et al., 2017). Power generation systems using supercritical fluids are therefore able to a large output from a single power plant. A test of the capacity of supercritical fluids (wellhead temperature of 450°C) from IDDP-1 in Krafla revealed that the energy output was 10-fold higher than that of conventional wells (Elders et al., 2014).

Gaining an in-depth understanding of the spatial distribution and fluid fraction of supercritical geothermal reservoirs is necessary for their assessment as an unconventional energy resource (Reinsch et al., 2017; Stimac et al., 2017). Deep drilling can be used to calculate the amount of available resources of supercritical fluids (Doi et al., 1998; Elders et al., 2014; Fournier, 1999; Friðleifsson et al., 2020; Ikeuchi et al., 1998). In one drill expedition, a core sample of the Kakkonda granite in the WD-1a well near the bottom (3729 m depth) was found to have a porosity of 1.7% (Muraoka et al., 1998). However, as a method to assess supercritical geothermal systems, deep drillings are expensive (Elders et al., 2014). Owing to the limited number of deep drilling points, the distribution and fluid fraction of supercritical geothermal reservoirs remain poorly understood. Therefore, geophysical methods (e.g. electromagnetic and seismic methods) are required to gain insights into the spatial distribution and fluid fraction of supercritical geothermal reservoirs (Piana Agostinetti et al., 2017; Reinsch et al., 2017).

In this study, we used the magnetotelluric (MT) method with electrical resistivity imaging to calculate the spatial distribution and fluid fraction of a supercritical geothermal reservoir in NE Japan. The MT method is suitable for measuring the spatial distribution and fluid fraction of subsurface fluids because electrical resistivity is sensitive to the existence of fluids (Comeau et al., 2020; Ogawa et al., 2014; Unsworth et al., 2005; Wannamaker et al., 2009). The fluid fraction of a supercritical geothermal reservoir was obtained from a resistivity model using MT data. For the estimation of the fluid fraction, we assumed that the supercritical geothermal reservoir consisted of solid rock and supercritical fluid in the solid-rock pore, and that the supercritical fluid saturated the pore. The resistivity obtained using the MT method is bulk resistivity, which includes contributions from the solid rock and supercritical fluid in the pore (Chave & Jones, 2012; Hashin & Shtrikman, 1962). However, the contribution of solid rock resistivity to bulk resistivity is limited (Ogawa et al., 2014), indicating that if the resistivity of a supercritical fluid is known, we can obtain the fluid fraction of a supercritical geothermal reservoir from the bulk resistivity. We considered magmatic supercritical fluids as NaCl-H_2O fluids because magmatic fluids mainly consist of water and chloride salts (Blundy et al., 2021; Heinrich, 2005; Monecke et al., 2018; Richards, 2011; Sillitoe, 2010). The electrical resistivity of NaCl-H_2O fluids has been studied extensively in the relationship between subsurface resistivity models and geological structures (Bannard, 1975; Nono et al., 2020; Quist & Marshall, 1968; Sakuma & Ichiki, 2016; Sinmyo & Keppler, 2016). Bannard (1975) measured the resistivity of NaCl-H_2O fluids for a wide range of pressure, temperature, and NaCl conditions, including supercritical conditions (up to 200 MPa, 525°C, and 25 wt%). Thus, we used the resistivity values of NaCl-H_2O fluids reported by Bannard (1975) for the resistivity of supercritical fluids.

NE Japan can be classified as a typical subduction zone, where the Pacific plate subducts beneath the land area at a rate of ~10 cm/year (Hasegawa et al., 1991). The dehydration of the subducting slab in the mantle wedge results in the upward migration of fluids (Tatsumi, 1989).

Upwelling hot fluids from the mantle wedge were detected by low-velocity anomalies of S-wave (so-called "hot fingers"). These hot fingers are distributed over NE Japan at intervals of several tens of kilometers (Tamura et al., 2002) and indicate that a large number of supercritical fluid reservoirs may exist in NE Japan (Okamoto et al., 2019). We selected the Yuzawa geothermal field in NE Japan as the target area. Hot fingers exist around this geothermal field (Tamura et al., 2002). Other geophysical and geochemical data (e.g. thermoluminescence, borehole temperature, and seismic data) also suggest that supercritical fluids may exist at a depth of a few kilometers (New Energy and Industrial Technology Development Organization, 1990; Nunohara et al., 2021; Okada et al., 2014). We conducted an MT survey to reveal the spatial distribution and fluid fraction of a potential supercritical geothermal reservoir in this field. Any information obtained on a supercritical geothermal reservoir in this field is likely to be useful for the estimation of spatial distribution and fluid fraction of other supercritical geothermal reservoirs in NE Japan (e.g. Naruko, Onikobe, and Kakkonda areas). Here, we first provide a brief introduction of the Yuzawa geothermal field and MT method. Then, we present our findings on the estimation of the spatial distribution of a potential supercritical reservoir and its fluid fraction.

2. Yuzawa geothermal field in NE Japan

The Yuzawa geothermal field in NE Japan contains one of the largest geothermal systems in Japan (Nunohara et al., 2021). This field is located in the inner part of the Sanzugawa caldera (Figures 1a and 1b). The Sanzugawa caldera, which was first formed ca. 3 My ago, has a size of 30 km north-south and 20 km east-west (Takeno, 2000). A Quaternary volcano, the Takamatsu volcano, or Takamatsu-dake, is found in this geothermal field (red star in Figures 1b and 1c). The Takamatsu volcano is located 40 km west of the volcanic front (Tamanyu et al., 1998). The volcano is composed of calc-alkaline andesite to dacite. The age of this volcano was estimated to be 0.2–0.3 My by thermo-luminescence and K–Ar methods (Umeda et al., 1999). The magma below the volcano is considered to be the heat source of this geothermal field (Takeno, 2000). Geothermal features, such as hot springs and hydrothermally altered rocks, have been observed extensively at the surface in this geothermal field, indicative of a well-developed hydrothermal system (Nunohara et al., 2021). Two geothermal power plants (Uenotai: 28,500 kW and Wasabizawa: 46,200 kW) are currently in operation using a hydrothermal system at temperatures <300°C (Figure 1c).

Seismic imaging of NE Japan suggests that upwelling fluids exist beneath this geothermal field at a depth of up to several kilometers (Nakajima et al., 2001; Okada et al., 2014; Tamura et al., 2002). The high He^3/He^4 in this field also indicates that fluids upwell to the surface from the upper mantle (Horiguchi et al., 2010; Kita et al., 1992). Drillings conducted by the New Energy and Industrial Technology Development Organization (NEDO) revealed that the thermal gradient of the conduction-dominated profile at N63-MS-6 (blue square in Figure 1c) was 170°C/km (New Energy and Industrial Technology Development Organization, 1990). This thermal gradient suggests that temperatures can reach >400°C at a depth of 2.5 km. These geophysical observations strongly indicate the possible existence of a supercritical geothermal reservoir (>400°C) in this field.

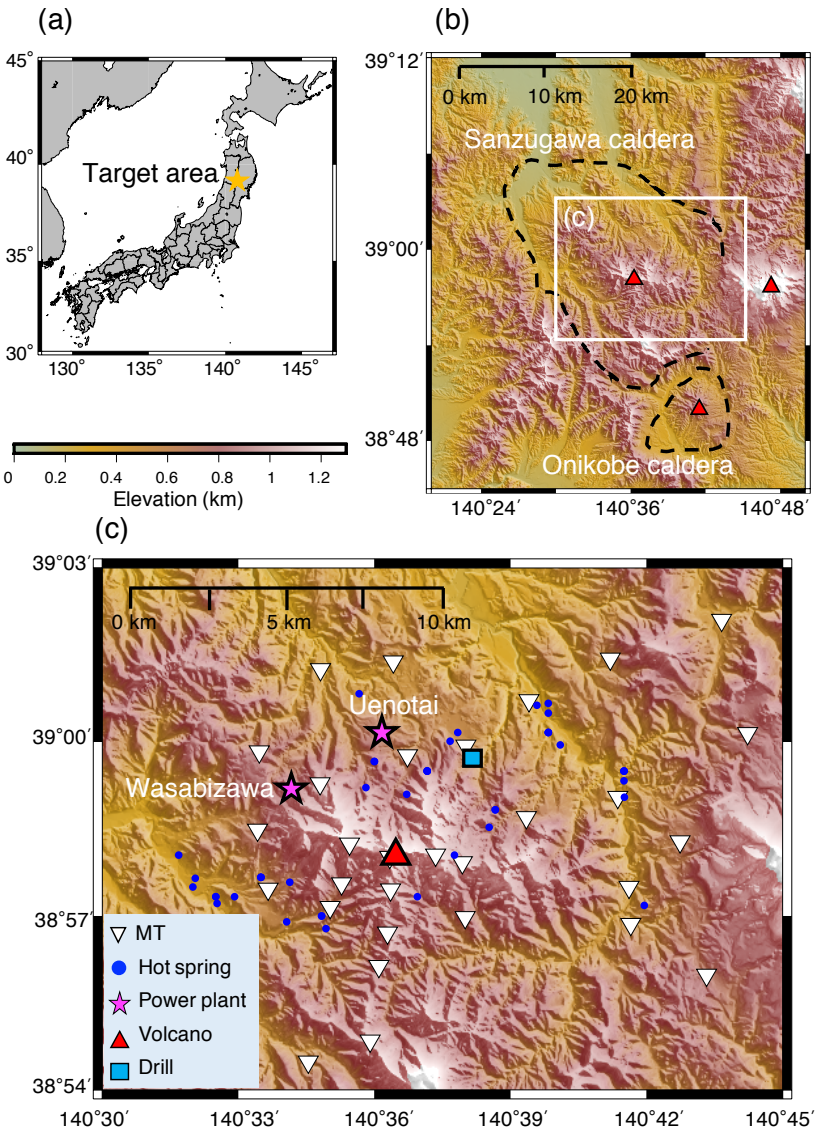

Figure 1. Maps of the study area. (a) Location of the Yuzawa geothermal field, NE Japan (orange star). (b) Regional map around the Yuzawa geothermal field. Dotted lines follow the outline of the calderas (Yoshida et al., 2014). Red triangles denote the major Quaternary volcanoes. (c) Local map of the Yuzawa geothermal field. White triangles denote MT sites. Blue circles denote hot springs. Magenta stars denote power plants (Uenotai: 28,500 kW and Wasabizawa: 46,200 kW). The red triangle denotes the Takamatsu volcano. The light blue square denotes the NEDO drilling site (N63-MS-6), reaching a depth of 1500 m (New Energy and Industrial Technology Development Organization, 1990).

3. Methods

The MT method is a geophysical tool used to map the electrical resistivity structure of subsurfaces (Araya Vargas et al., 2019; Árnason et al., 2010; Becken et al., 2011; Bedrosian et al., 2018; Di Paolo et al., 2020; Heinson et al., 2018; Heise et al., 2008; Hyndman & Shearer, 1989; Ichihara et al., 2016; Ingham et al., 2009; Le Pape et al., 2015; Moorkamp et al., 2019; Wise & Thiel, 2020). This method uses surface measurements of naturally occurring low-

frequency electromagnetic variations to infer subsurface resistivity structures (Chave & Jones, 2012). Each MT station observes two electric field components (E_x and E_y) and three magnetic field components (H_x, H_y, and H_z). The x, y, and z directions are consistent with the geographic north, east, and vertical depths, respectively. The observed data were analyzed using the impedance tensor **Z** and tipper **T**, as follows:

$$\begin{bmatrix} E_x \\ E_y \\ H_z \end{bmatrix} = \begin{bmatrix} Z_{xx} & Z_{xy} \\ Z_{yx} & Z_{yy} \\ T_{zx} & T_{zy} \end{bmatrix} \begin{bmatrix} H_x \\ H_y \end{bmatrix}. \quad \textbf{(1)}$$

The complex impedance tenser in the frequency domain is expressed in terms of the apparent resistivity and phase for data interpretation (Chave & Jones, 2012). The complex impedance tensor is also expressed as a phase tensor since phase tensor is independent of the distorting effects produced by localized near-surface resistivity heterogeneities (Caldwell et al., 2004).

The observed MT data were converted into a surface-to-subsurface resistivity model using inversion analysis (Constable et al., 1987; Farquharson, 2008; Kelbert et al., 2014; Newman, 2014; Ogawa & Uchida, 1996; Siripunvaraporn & Egbert, 2009). We used WSINV3DMT for the three-dimensional (3D) inversion of the observed MT data (Siripunvaraporn & Egbert, 2009). WSINV3DMT seeks to minimize the function as follows:

$$U = (\boldsymbol{m} - \boldsymbol{m}_0)^T \mathbf{C}_m^{-1} (\mathbf{m} - \mathbf{m}_0) + \lambda^{-1} \{ (\mathbf{d} - \mathbf{F}[\mathbf{m}])^T \mathbf{C}_d^{-1} (\mathbf{d} - \mathbf{F}[\mathbf{m}]) - \chi_*^2 \}, \quad \textbf{(2)}$$

where **m** is the resistivity model, $\mathbf{m}_0$ is the prior model, **d** is the observed data, **F**[**m**] is the forward modeling response, $\mathbf{C}_m$ is the model covariance, $\mathbf{C}_d$ is a data covariance matrix, χ_* is the desired level of misfit, and λ^{-1} is a Lagrange multiplier. WSINV3DMT penalizes smoothed deviations from a prior model with spatial covariance. Thus, the obtained resistivity model by the regularized MT inversion is the smooth model away from a prior model.

4. Results

We collected MT data at 30 measurement sites to image resistivity structures in the Yuzawa geothermal field (Figure 1c). Since the objective of this study is to image supercritical geothermal reservoirs at depths of several kilometers, the MT site spacing is several kilometers. The phase tensor ellipses at 20 Hz showed higher phase values around Takamatsu volcano and power plants (Figure 2a). The phase tensor data suggest the existence of near-surface conductors. The phase tensor showed increased values at 2.5 Hz and decreased values at 0.3 Hz, which implies the presence of a deep conductor (Figure 2). The impedance and tipper data for each observation site are shown in Figure S1–S6.

Inverse modeling with WSINV3DMT converted the observed MT data into 3D resistivity structures (Siripunvaraporn et al., 2005; Siripunvaraporn & Egbert, 2009). The initial resistivity model for inverse modeling consisted of the subsurface (100 ohm-m), ocean (0.3 ohm-m), and air (10^{10} ohm-m). The prior resistivity model was set to be the same as the initial resistivity model. The computational grid consisted of 74 × 74 × 70 cells, including boundary cells. In the central region of the model (–10 km < x and y < 10 km), the mesh had a regular cell size of 300 m in the horizontal direction. Outside this central region, the horizontal mesh size increased with increasing distance from the central region. For elevations between 1.3 km and 0 km, we set the vertical mesh size to values ranging from 20 m to 50 m. Note that elevation is indicated as height

above sea level in this study. For elevations below 0 km, the mesh size increased with an increasing depth. The computations of the inverse modeling were performed on a computer (@Xeon 3.10 GHz Gold 6254 central processing unit; Intel Corp.) with 3 TB of RAM. The impedance tensor and tipper between frequencies of 0.001–100 Hz (17 frequencies) were used for inverse modeling. Error floors of 5% for the impedance tensor and 15% for the tipper were used. The root-mean-square (RMS) misfit for the initial model was 10.2. The inversion analysis obtained a resistivity model with an RMS misfit of 2.34 after three iterations (Figure 3). The data fits were good for almost all sites and frequencies (Figure S1–S6).

3D resistivity structures obtained from the inverse modeling identified a near-surface conductor at an elevation between 1.3 and –0.5 km, as well as a deep conductor C1 at an elevation between –1.5 and –12 km (Figure 3). The resistivity of the near-surface conductor was 5–20 ohm-m, which was lower than that of the surrounding rock of 100 ohm-m. Near-surface conductors were widely distributed in this area. The resistivity value of C1 was approximately 10 ohm-m. These low resistivity anomalies are consistent with the features of the observed data (Figure 2 and Figure S1–S6). C1 was imaged northeast of Takamatsu volcano and not immediately below the volcano. The size of C1 was 3 km (width) × 5 km (length) × 10 km (height). Conductive zones extended from the east and west ends of deep conductor C1 to the near-surface conductors (Figure 3c). The conductor zone extending from the west end of C1 extended towards the Wasabizawa power plant (Figure 3c). Although a deep conductor was imaged at y = 9 km outside the coverage area of the receiver (Figure 3c), the MT data did not sufficiently constrain resistivity structures outside the coverage area of the receiver. Therefore, we have excluded this conductor from our discussions in this study.

The deep conductor C1 is potentially related to a supercritical fluid reservoir. It is known that the MT method is uncertain, especially for deep resistivity structures, such as C1 (Ishizu et al., 2021). We calculated the MT responses for models where the resistivity value of C1 was replaced by 1–100 ohm-m to determine how well this resistivity value was constrained by the data (Figure S7). The RMS misfit was minimum for 10 ohm-m and increased away from 10 ohm-m (Figure S7). Reliability was measured based on F values with a 95% confidence interval (Gresse et al., 2021; Yamaya et al., 2017). The threshold RMS misfit with a 95% confidence interval was 2.392. Forward models associated with C1: 6.5 ohm-m < C1 < 35 ohm-m obtained a RMS misfit <2.392. Forward models associated with low and high resistivities (i.e. <6.5 ohm-m and >35 ohm-m) showed RMS values higher than F_{RMS} = 2.392. In other words, these forward models were statistically rejected with a 95% confidence interval. Hence, we conclude that the resistivity range of C1 is 6.5 ohm-m < C1 < 35 ohm-m.

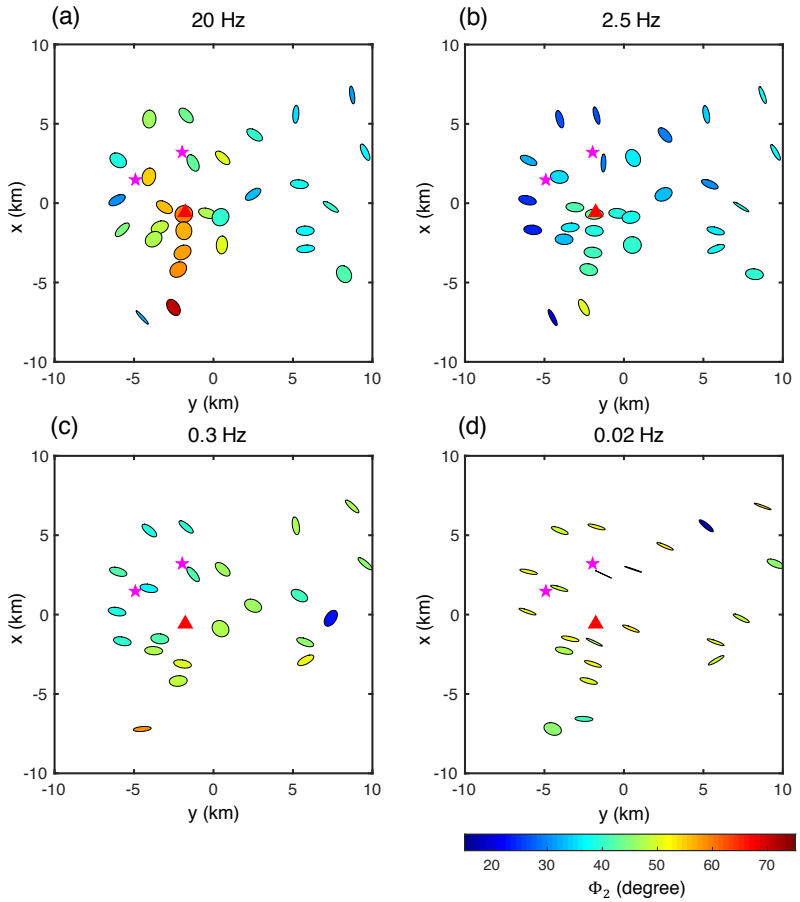

Figure 2. Phase tensor ellipses of observed MT data for (a) 20 Hz, (b) 2.5 Hz, (c) 0.3 Hz, and 0.02 Hz. The phase tensor ellipses are filled by $\tan^{-1}(\Phi_2)$, where Φ_2 is the geometric mean of the diagonal components of the phase tensor components (Φ_{max} and Φ_{min}) (Caldwell et al., 2004). Phase tensor ellipses have been normalized by the maximum phase value. Magenta stars denote power plants. The red triangle denotes Takamatsu volcano. Note that *x* and *y* directions are consistent with the geographic north and east, respectively.

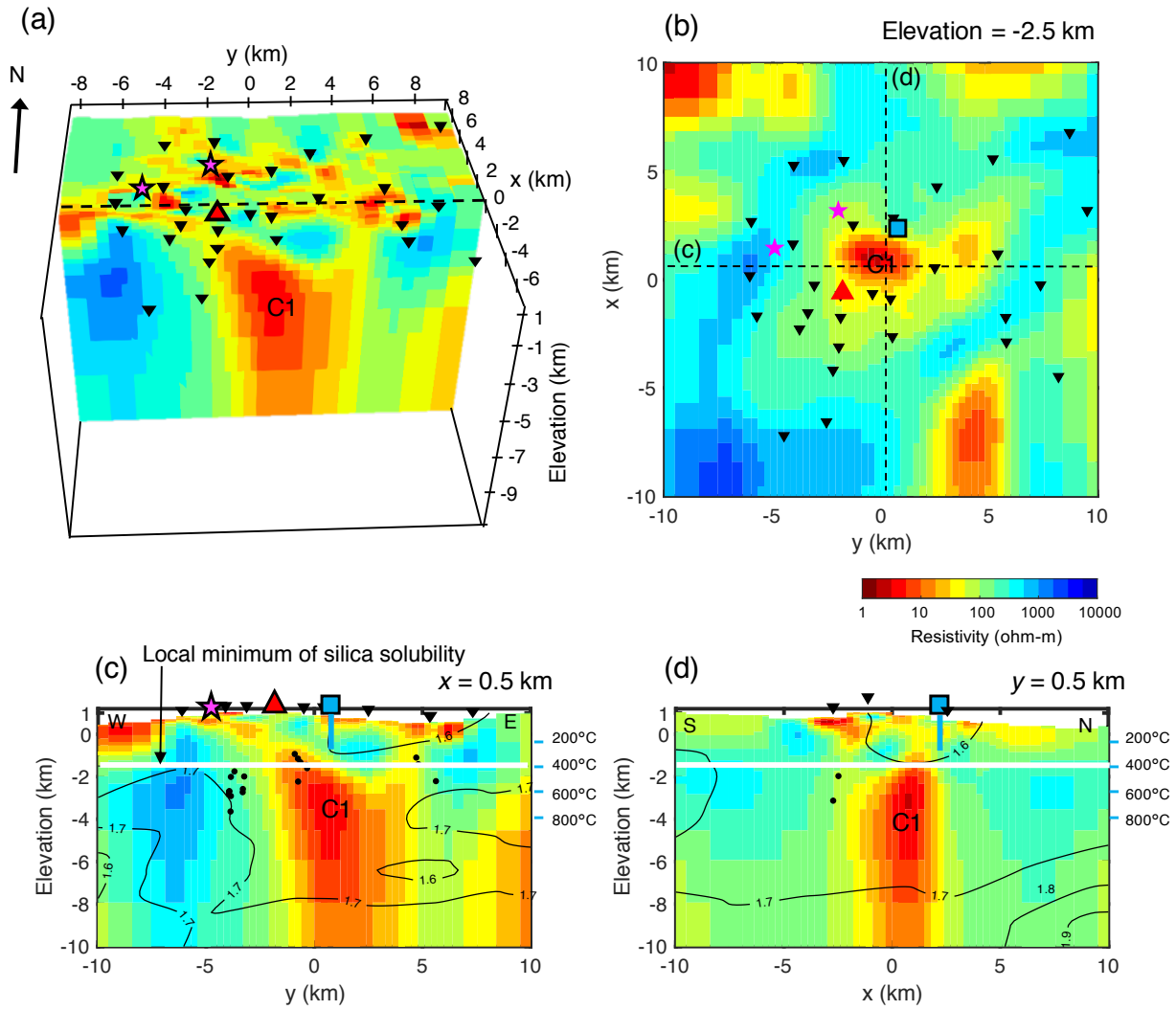

Figure 3. (a) 3D view with vertical slice at x = 0.5 km; (b) horizontal slice at an elevation of –2.5 km; (c) vertical slice at x = 0.5 km; (d) vertical slice at y = 0.5 km of the inverted resistivity model from the MT data. C1 denotes conductive zones, which imply a supercritical fluid and partial melting. Black triangles denote MT sites. Magenta stars denote power plants. The red triangle denotes Takamatsu volcano. The light blue square denotes the NEDO drilling sites (N63-MS-6). Contours of Vp/Vs ratio (Okada et al., 2014) are superimposed on the sections in (c) and (d). Black triangles denote MT sites within ±1 km of each profile line. Black dots denote the relocated hypocenters of earthquakes within ±150 m of each profile line (Okada et al., 2014). White lines denote the depth of a local minimum of silica solubility, as presented in Figure 5. Note that elevation is indicated as height above sea level, and x and y directions denote the geographic north and east, respectively.

5. Discussion

5.1 Shallow hydrothermal system

Initially, a shallow geothermal system was investigated using the obtained resistivity model. The resistivity model revealed the near-surface conductor at an elevation greater than –0.5 km (Figure 3). Similar near-surface conductors found in various volcanic areas have been interpreted as smectite-rich zones (Cherkose & Saibi, 2021; Kanda et al., 2019; Ledo et al., 2021; Tseng et al., 2020; Yoshimura et al., 2018). Drilling confirmed the smectite-rich zones in this field (New Energy and Industrial Technology Development Organization, 1990). Moreover, the distribution of near-surface conductors was consistent with the distribution of hydrothermal alteration zones on the surface (Nunohara et al., 2021). These results indicate that the near-surface conductor was a smectite-rich zone. Furthermore, the bottom of the near-surface conductors was roughly consistent with the isotherm at 200°C (Figure 3d). Smectite under moisture-rich conditions can be converted to illite at temperatures exceeding 200°C (Wersin et al., 2007; Yamaya et al., 2013). The resistivity of illite was much higher than that of smectite (Ussher et al., 2000). Hence, we interpreted the resistive zone below the near-surface conductors as an illite-rich zone transformed from smectite above 200°C.

Conductive zones were found to extend from the east and west ends of deep conductor C1 to the near-surface conductors (Figure 3c). The conductor zone extending from the west end of C1 extended towards the Wasabizawa power plant (Figure 3c). The $^{3}He/^{4}He$ and $^{4}He/^{20}Ne$ ratios of the fumarolic gas at the Kawarage hot spring, located 3 km west of the Wasabizawa power plant, were 9.5×10^{-6} and 180, respectively (Kita et al., 1992). This indicates that the helium at the Kawarage hot spring originated from magmatic gas. These results suggest that these conductive zones act as a path for magmatic fluid ascending from C1, resulting in anomalies in the helium ratios at the Kawarage hot spring. A conductor extending from the deep parts (25 km depth) to the surface at Naruko volcano also represented a path for ascending magmatic fluid (Ogawa et al., 2014).

5.2 Supercritical geothermal reservoir

The low resistivity of C1 suggests that it includes fluids (magmatic fluids and melts). The geometry of C1 is consistent with low Vp and Vs zones, supporting that C1 contains magmatic fluids and melts (Figure S8). The temperature of C1 was estimated to be above 400°C based on the temperature profile (Figure 4a). While a few seismicities occurred inside C1, most occurred around the edge of C1 (Figure 3). The depth of the seismicity cut-off was consistent with that of C1, and it is known that the depth of the seismicity cut-off roughly corresponds to 400°C (Mitsuhata et al., 2001; Ogawa et al., 2001; Okada et al., 2014). The correspondence between the top of C1 and the seismicity cut-off also supports that C1 was >400°C.

Similar conductors at depths of 2–15 km in other volcanoes have been interpreted as magmatic fluids and melts depending on the temperature and pressure (e.g., Mount St Helens: Bedrosian et al., 2018, Geysers: Peacock et al., 2020, Laguna del Maule: Cordell et al., 2020, Kirishima: Aizawa et al., 2014; Taupo: Bertrand et al., 2012, Krafla: Lee et al., 2020). A minimum solidus temperature of 725°C at a pressure of 100 MPa (Bowles-Martinez & Schultz, 2020; Tuttle & Bowen, 1958), suggested that the part of C1 at a temperature lower than 725°C was comprised of magmatic fluid. The thermal gradient of 170°C/km suggests that the temperature at an elevation of −4 km becomes 725°C (Figure 4a). Therefore, we considered the upper part of C1 at an

elevation greater than −4 km as a potential supercritical fluid reservoir (>400°C) instead of melt. The low Vp/Vs ratio (<1.7) in the upper parts of C1 (Figure 3 and Figure S8) also indicated that the upper parts were mainly magmatic fluid instead of melt (Okada et al., 2014).

NaCl-H_2O fluids can be found in different phases depending on the pressure, temperature, and salinity conditions (Afanasyev et al., 2018; Driesner & Heinrich, 2007; Sillitoe, 2010; Weis et al., 2012). Three fluid phases (1: single-phase, 2: vapor-liquid coexisting phase, 3: vapor-halite coexisting phase) can be expected for supercritical fluids (Figure 5a). The fluid phase can affect the resistivity of the NaCl-H_2O fluids. The typical NaCl content of magmatic fluids is 5–10 wt%, based on fluid inclusion analysis (Heinrich, 2005). Recent mantle xenolith studies reported the NaCl content of fluids in the mantle wedge to be 5.1 wt% (Kawamoto et al., 2013). First, we consider that the magmatic fluid has a 5 wt% NaCl equivalent. The pressure at the potential supercritical reservoir is expected to be hydrostatic or lithostatic, or somewhere between the two (Figure 4b). We calculated the hydrostatic pressure assuming a water density of 1000 kg/m^3 and lithostatic pressure assuming a rock density of 2700 kg/m^3 (Saishu et al., 2014).

We consider the fluid phase of the reservoir top at an elevation of −1.8 km (temperature of 450°C) because shallow parts are easier to exploit than deeper parts. The phase of the supercritical fluid is a vapor-halite coexisting phase at 450°C if the pressure is in the hydrostatic condition (Figure 5a). We assumed that the halite is resistive at >10^8 ohm-m (Watanabe & Peach, 2002), while the vapor is resistive at 1000 ohm-m (Peacock et al., 2020). As a result, the vapor-halite coexisting phase is estimated to be much more resistive than the 10 ohm-m of C1. The phase of the supercritical fluid is a vapor-liquid coexisting phase at 450°C if the pressure is below the average between hydrostatic and lithostatic conditions (e.g. 35 MPa) (Figure 5a). In the vapor-liquid coexisting phase, the fluid exists as low-salinity vapor in equilibrium with a small fraction of hypersaline brine (Driesner & Heinrich, 2007). Despite a lack of laboratory measurement data for the resistivity of the vapor-liquid coexisting phase, to the best of our knowledge, the two-phase zones have been reported as resistive zones of 100–1000 ohm-m (Gresse et al., 2021; Samrock et al., 2018), which are much more resistive than 10 ohm-m of C1. The phase of the supercritical fluid is single-phase at 450°C if the pressure is in the lithostatic condition (Figure 5a). Bannard (1975) showed that the resistivity of a single phase is low. If we consider a single-phase supercritical fluid under pressure close to the lithostatic pressure, 10 ohm-m can be reasonably explained. Therefore, the supercritical fluid was considered as a single-phase fluid under pressure close to the lithostatic pressure. Although the magmatic fluid was considered to have a 5 wt% NaCl equivalent, a higher pressure close to the lithostatic pressure was also predicted for the magmatic fluid with 10 wt% NaCl equivalent to a single-phase (Figure 5b).

If a connection exists to the surface from the supercritical fluid reservoir, the pressure should be under hydrostatic conditions in the supercritical fluid reservoir. Hence, sealing to weaken the connections should be considered as an explanation for the lithostatic pressure of the reservoir (Scholz, 2019; Sibson, 2020). Silica sealing has been found above the potential supercritical reservoir and may separate the hydrostatic and lithostatic regions (Fournier, 1999; Ingebritsen & Manning, 2010; Lowell et al., 1993; Manning, 1994; Saishu et al., 2014; Weatherley & Henley, 2013). To consider the potential of silica sealing in this field, we calculated the silica solubility using Loner AP software (Akinfiev & Diamond, 2009). The quartz solubility had a local minimum for hydrostatic pressure, indicating that quartz precipitation could occur at this depth from downward-moving fluids (surface to deep) (Figure 6). The depth of the local minimum was

365 consistent with that of the top of C1. This suggests that silica sealing exists above C1. After the
366 development of silica sealing by downward-moving fluids with hydrostatic pressure, the
367 developed silica sealing weaken the connection from the supercritical fluid reservoir to the
368 surface. Moreover, upward-moving fluids with lithostatic pressure from the deep parts of the
369 crust can enhance the sealing if the upward-moving fluid encounters the fluids with hydrostatic
370 pressure due to differences in their silica solubility (Fournier, 1999; Saishu et al., 2014). These
371 mechanisms can explain why the silica sealing developed there and separate the hydrostatic and
372 lithostatic regions (Figure 4c). The silica sealing also plays a role in trapping the upwelling
373 supercritical fluids due to its low permeability.

374 We considered the fluid fraction of a potential supercritical reservoir using the obtained
375 resistivity model. We assumed that the potential supercritical reservoir is comprised of a
376 complex (supercritical fluid and solid phase). The bulk resistivity of the potential supercritical
377 reservoir was modeled using the Hashin–Shtrikman upper bound model (HS+) (Hashin &
378 Shtrikman, 1962). We used the resistivity values of NaCl-H_2O fluids reported by Bannard (1975)
379 for the resistivity of supercritical fluid. The solid-phase resistivity was fixed at 1000 ohm-m.
380 Reservoir pressure was assumed to be under the lithostatic condition (Figure 4c). For the C1 top
381 at an elevation of –1.8 km (450°C and 60 MPa), 10 ohm-m resistivity of C1 required a fluid
382 fraction of 1% and 0.5% for 5 wt% and 10 wt% NaCl equivalent, respectively (Figure 7). Ishizu
383 et al. (2021) found that MT inversion often overestimates the resistivity of deep conductors by
384 modeling studies (i.e. the estimated resistivity is higher than the true resistivity). Thus, the true
385 resistivity of C1 is expected to be lower than 10 ohm-m. If we consider the lower bound *F* value
386 (6.5 ohm-m), the fluid fractions are 2% and 1% for 5 wt% and 10 wt% NaCl equivalent,
387 respectively (Figure 7). The 0.5–2% fluid fraction of the potential supercritical fluids estimated
388 by the resistivity model was consistent with the porosity (1.7%) of the core sample of the
389 Kakkonda granite near the bottom of the WD-1a well (Muraoka et al., 1998). The resistivity of
390 supercritical fluids depends on the temperature and pressure (Bannard, 1975; Nono et al., 2020).
391 Although measurement data of the resistivity values of NaCl-H_2O fluids at higher temperatures
392 and pressures (e.g. 600°C and 100 MPa) is lacking, the resistivity was predicted to be higher than
393 that at 450°C and 60 MPa, according to the measurements reported by Bannard (1975). This
394 indicates that a fluid fraction higher than 0.5–2% is predicted for the bottom of the reservoir.
395 However, the bottom of the supercritical reservoir is not currently economically exploitable
396 because of the low permeability and high cost of deep drilling (Watanabe et al., 2017).

397

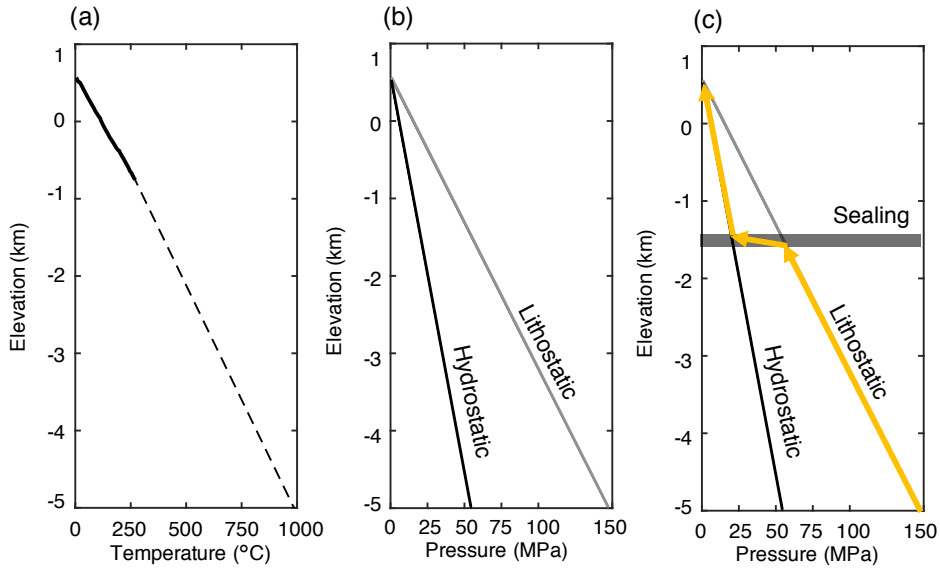

Figure 4. (a) Temperature profile as a function of elevation at the NEDO drilling sites (N63-MS-6), as presented in Figure 1b (New Energy and Industrial Technology Development Organization, 1990). The solid line denotes logging data and the dashed line denotes the extrapolated profile. (b) The pressure profile as a function of elevation under hydrostatic pressure (black line) and lithostatic pressure (grey line), respectively. We calculated the hydrostatic pressure assuming a water density of 1000 kg/m^3 and lithostatic pressure assuming a rock density of 2700 kg/m^3 (Saishu et al., 2014).

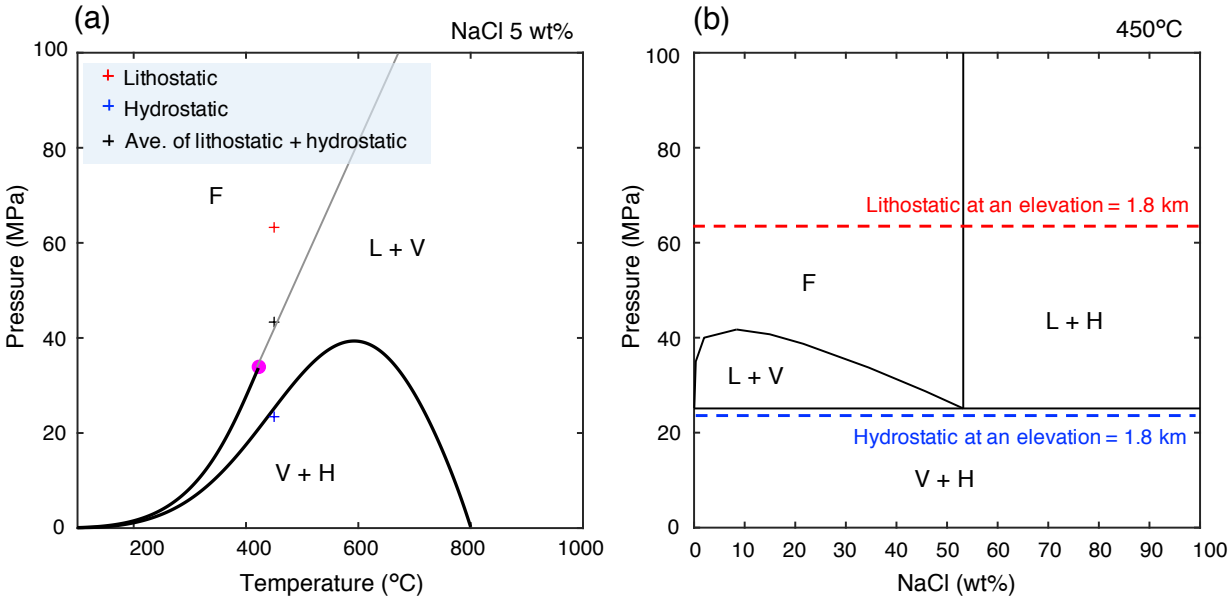

Figure 5. (a) Pressure-temperature diagram of NaCl-H_2O solution for 5 wt% NaCl equivalent, calculated using AqSo_NaCl software (Bakker, 2018). The magenta circle denotes the critical point (422°C and 34 MPa). Red, blue, and black crosses denote the pressure-temperature points at an elevation of –1.8 km (450°C) under lithostatic, hydrostatic, and average of lithostatic and hydrostatic, respectively. (b) Isothermal pressure–composition sections for 450°C. The red and

blue lines denote pressure at an elevation of –1.8 km under hydrostatic and lithostatic conditions. L, liquid, V, vapor, H, halite; for temperatures equal to or higher than the critical temperature of the fluid, the notation F, fluid was introduced to underline that those fluid properties can gradually change from liquid-like to vapor-like without crossing a phase boundary in this region (Driesner & Heinrich, 2007).

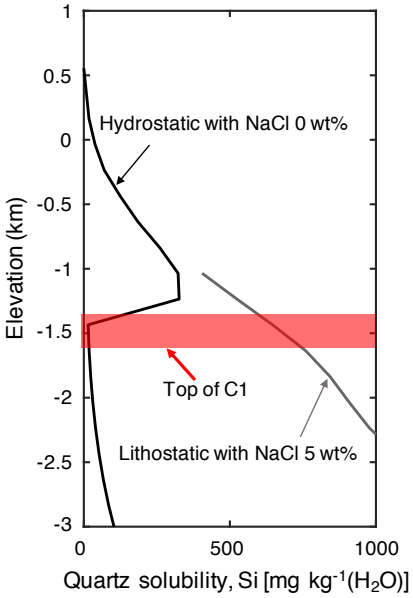

Figure 6. Quartz solubility profiles as a function of depth, calculated using Loner AP software (Akinfiev & Diamond, 2009). The solubility for pure H_2O under hydrostatic conditions (salinity = 0 wt%; black line) and the solubility for saline fluid under lithostatic conditions (5 wt% NaCl equivalent; grey line) are shown. The red dashed line denotes the top of C1, as shown in Figure 3.

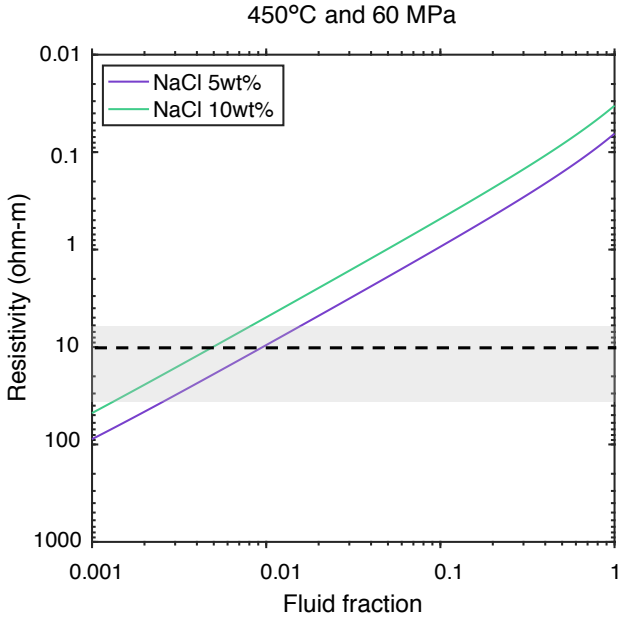

426 **Figure 7.** The bulk resistivity of the complex (supercritical fluid and solid phase) at 450°C and
427 60 MPa as a function of fluid fraction and of NaCl content in the supercritical fluid. Supercritical
428 fluid resistivity was calculated based on the laboratory measurement results of Bannard (1975).
429 Bulk resistivity was calculated using Hashin–Shtrikman upper bound model (*HS*+) (Hashin &
430 Shtrikman, 1962). Solid phase resistivity was fixed at 1000 ohm-m. The gray zone denotes the
431 resistivity range with a 95% confidence interval for C1 based on *F*-test (6.5 ohm-m < C1 < 35
432 ohm-m).
433

434 **5.3. Partial melt**

435 The temperature at an elevation lower than –5 km was estimated to be above 800°C. This
436 temperature of 800°C was over the minimum solidus temperature of 725°C at a pressure of 100
437 MPa for silicic melts (Bowles-Martinez & Schultz, 2020; Tuttle & Bowen, 1958). Therefore, C1
438 may include a melt at an elevation lower than −5 km. Resistivity models are useful for inferring
439 the melt fraction in the subsurface (Feucht et al., 2017; Hata et al., 2015; Hill et al., 2009; Ichiki
440 et al., 2021; Lee et al., 2020; Peacock et al., 2015; Piña-Varas et al., 2018; Samrock et al., 2018).
441 The resistivity of the melt has been well studied in the literature (Gaillard & Marziano, 2005;
442 Guo et al., 2017; Laumonier et al., 2015; Pommier & Le-Trong, 2011). Here, we assume that the
443 part of C1 with a temperature above 800°C consists of a complex (melt and solid phase).

444 A petrologic study revealed that dacitic and andesitic melts are likely to exist in this field (Ban et
445 al., 2007). The dacitic melt has a shallower origin than the andesitic melt (Ban et al., 2007;
446 Tatsumi et al., 2008). We assume that conductor C1 at an elevation of −5 km consists of the
447 complex (dacitic melt and solid phase), and used the resistivity value reported by Laumonier et al.
448 (2015) for dacitic melt. Bulk resistivity was calculated using the Hashin–Shtrikman upper bound
449 model (HS+) (Hashin & Shtrikman, 1962) The solid-phase resistivity was fixed at 1000 ohm-m.
450 The bulk resistivity of the complex (dacitic melt and solid phase) at 900°C and 150 MPa (−5 km
451 elevation) suggests that an 80% melt fraction with 2 wt% H_2O is required to explain the 10 ohm-
452 m of C1. As mentioned above, the MT method may overestimate the resistivity values (Ishizu et
453 al., 2021). If we consider the lower bound of C1 (6.5 ohm-m), the 100% melt fraction is
454 considered for 2 wt% H_2O. However, these melt fractions are not reasonable. The water content
455 in the dacitic melt can range up to 5.5 wt%, which is the water saturation condition (Wallace,
456 2005). If the dacitic melt was almost water-saturated (5 wt% H_2O), the 20% melt fraction could
457 explain 10 ohm-m. Even if we consider the lower bound of C1 (6.5 ohm-m), the 30% melt
458 fraction was considered for 5 wt% H_2O. These findings suggest that C1 at an elevation of −5 km
459 is a dacitic melt with 5 wt% H_2O and a melt fraction of 20–30%.

460 The andesitic melt is expected to be located in the deep zones of this field (Ban et al., 2007). The
461 conductor C1 at an elevation of –9 km was assumed to consist of a complex (andesitic melt and
462 solid phase). The resistivity of the andesitic melt was calculated according to Guo et al. (2017).
463 To explain 10 ohm-m of C1 at 1050°C and 250 MPa (–9 km elevation), the melt fraction was
464 estimated to be 2% for 8 wt% H_2O and 20% for 2 wt% H_2O. Hence, our resistivity model
465 suggests that C1 at an elevation of –9 km consists of an andesitic melt with a melt fraction below
466 20%.

467

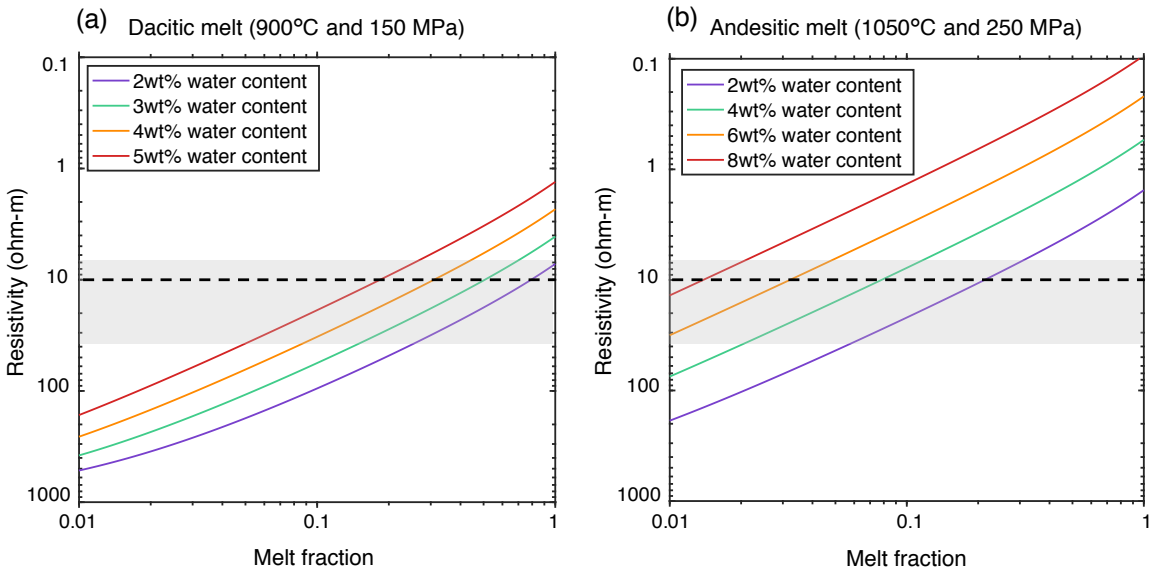

Figure 8. (a) The bulk resistivity of the complex (dacitic melt and solid phase) at 900°C and 150 MPa as a function of melt fraction and water content in the dacitic melt. The resistivity of the dacitic melt was calculated based on Laumonier et al. (2015). Solid phase resistivity was fixed at 1000 ohm-m. Bulk resistivity was calculated using Hashin–Shtrikman upper bound model (HS+). (b) The bulk resistivity of the complex (andesitic melt and solid phase) at 1050°C and 250 MPa as a function of melt fraction and water content in the andesitic melt. The resistivity of the andesitic melt was calculated based on Guo et al. (2017). The gray zones denote the resistivity range with a 95% confidence interval for C1 based on the *F*-test (6.5 ohm-m < C1 < 35 ohm-m).

5.4. Mechanism of evolution of a supercritical geothermal reservoir

Our MT data revealed a potential supercritical geothermal reservoir, a melt, and a shallow geothermal system in the Yuzawa geothermal field in NE Japan (Figure 3). Based on our resistivity model, we propose a mechanism for the evolution of a supercritical geothermal reservoir (Figure 9). The dacitic and andesitic melt below the supercritical geothermal reservoir may supply magmatic fluids to the supercritical geothermal reservoir (Blundy et al., 2021; Heinrich, 2005; Sillitoe, 2010). Upwelling supercritical fluids supplied from the melt were found to become trapped under a less-permeable silica sealing, and supercritical fluids accumulated below the silica sealing as a result (Figure 9). Silica sealing separates the hydrostatic and lithostatic regions (Figure 4c). Hence, the supercritical geothermal reservoir below the silica sealing is under lithostatic pressure, and the phase of the potential supercritical fluids is interpreted as a single phase. Single-phase supercritical fluids show low resistivity (Bannard, 1975). Therefore, the supercritical fluid reservoir was imaged as a low resistivity anomaly of C1 (Figure 3). The fluid fraction of the supercritical reservoir was estimated to be 0.5–2% (Figure 7). Episodic supplies of magmatic fluids from the melt increased the pressure of the supercritical fluid reservoir, with high levels of pressure subsequently breaking the silica sealing. Fluids leaking from the silica sealing moved to the surface (Figure 9). The fluids were detected as conductive zones extending from the deep conductor C1 to the near-surface conductors (Figure 3c). The smectite-rich zones near the surface act as an impermeable cap-to-trap hydrothermal fluid of mixed meteoric water and upwelling fluids owing to its low permeability (Revil et al.,

2019). Power plants in operation in the area use hydrothermal fluids (<300°C) trapped below the impermeable cap of smectite to generate electric energy (New Energy and Industrial Technology Development Organization, 1990). Since our MT data revealed a potential supercritical geothermal reservoir in this geothermal field, power plants in this field potentially may use supercritical geothermal reservoirs to increase their power generation in the future.

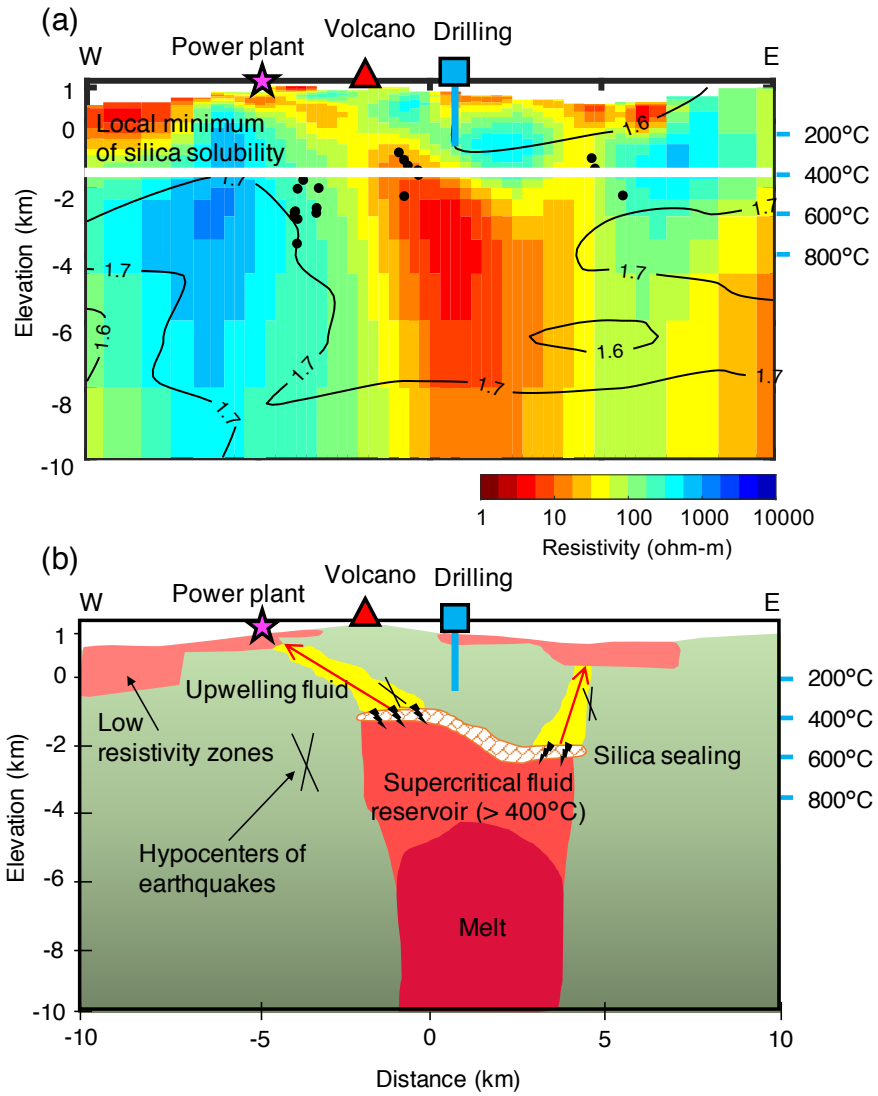

Figure 9. (a) West–east cross-section at x = 0.5 km of the inverted resistivity model. This cross-section is the same as Figure 3c. Symbols are the same as in Figure 3. (b) Schematic model of a geothermal system inferred from our resistivity model.

6. Conclusions

Supercritical geothermal reservoirs are next-generation energy resources that yield higher productivity than conventional geothermal fluids with temperatures <350°C. Despite the fact that understanding the fluid fraction and spatial distribution of supercritical geothermal reservoirs is

necessary for their assessment as a energy resource, these characteristics remain poorly understood. Therefore, to gain insights into the fluid fraction and spatial distribution of a supercritical geothermal reservoir, we applied the MT method in the Yuzawa geothermal field in NE Japan. As a result, this study is the first to present a detailed estimation of the spatial distribution and fluid fraction of a potential supercritical geothermal reservoir. Our main findings can be summarized as follows:

- The MT data revealed a supercritical geothermal reservoir, a melt, and a shallow geothermal system in the Yuzawa geothermal field.
- The MT data revealed a supercritical geothermal reservoir (>400°C) with a size of 3 km (width) × 5 km (length) at a depth of 2.5–6 km. The fluid fraction of the supercritical reservoir was estimated to be 0.5–2% with a salinity of 5–10 wt%.
- Silica sealing may exist above the potential supercritical geothermal reservoir, separating the hydrostatic and lithostatic regions. The potential supercritical fluids were considered to be under lithostatic pressure, and the fluid phase was interpreted as being single-phase.
- The MT data indicate that dacitic and andesitic melts exist below the supercritical fluid reservoir. The melt supplies magmatic fluid to the supercritical fluid reservoir.
- We propose a mechanism for the evolution of a supercritical fluid reservoir, wherein upwelling supercritical fluids supplied by the melt are trapped under less permeable silica sealing. As a result, supercritical fluids accumulate below the silica sealing.
- The supercritical fluid breaking from the silica sealing provides upward-moving fluids to the surface.

Acknowledgments

This work was supported by the Japan Society for the Promotion of Science KAKENHI (20K22326 and 21109003). We thank Prof. Weerachai Siripunvaraporn for allowing us to use the 3D MT inversion code and Prof. Tomomi Okada for providing seismic data and velocity models. We are grateful to Dr. Norihiro Watanabe for helpful discussions on the resistivity of supercritical fluids and Dr. Ryoichi Yamada for his help with the geological interpretation of the resistivity model.

Data Availability Statement

Data archiving is in progress, and the MT data used in this study will be available from the SPUD EMTF repository by the time this paper is accepted for publication. For the period of peer review, the MT data can be obtained from Supporting Information.

References

Afanasyev, A., Blundy, J., Melnik, O., & Sparks, S. (2018). Formation of magmatic brine lenses via focussed fluid-flow beneath volcanoes. *Earth and Planetary Science Letters*, *486*, 119–128. https://doi.org/10.1016/j.epsl.2018.01.013

Aizawa, K., Koyama, T., Hase, H., Uyeshima, M., Kanda, W., Utsugi, M., et al. (2014). Three-

dimensional resistivity structure and magma plumbing system of the Kirishima Volcanoes as inferred from broadband magnetotelluric data. *Journal of Geophysical Research: Solid Earth*, *119*(1), 198–215. https://doi.org/10.1002/2013JB010682

Akinfiev, N. N., & Diamond, L. W. (2009). A simple predictive model of quartz solubility in water–salt–CO2 systems at temperatures up to 1000°C and pressures up to 1000MPa. *Geochimica et Cosmochimica Acta*, *73*(6), 1597–1608. https://doi.org/10.1016/j.gca.2008.12.011

Araya Vargas, J., Meqbel, N. M., Ritter, O., Brasse, H., Weckmann, U., Yáñez, G., & Godoy, B. (2019). Fluid distribution in the Central Andes subduction zone imaged with magnetotellurics. *Journal of Geophysical Research: Solid Earth*, *124*(4), 4017–4034. https://doi.org/10.1029/2018JB016933

Árnason, K., Eysteinsson, H., & Hersir, G. P. (2010). Joint 1D inversion of TEM and MT data and 3D inversion of MT data in the Hengill area, SW Iceland. *Geothermics*, *39*(1), 13–34. https://doi.org/10.1016/j.geothermics.2010.01.002

Bakker, R. J. (2018). AqSo_NaCl: Computer program to calculate p-T-V-x properties in the H2O-NaCl fluid system applied to fluid inclusion research and pore fluid calculation. *Computers & Geosciences*, *115*, 122–133. https://doi.org/10.1016/j.cageo.2018.03.003

Bali, E., Aradi, L. E., Zierenberg, R., Diamond, L. W., Pettke, T., Szabó, Á., et al. (2020). Geothermal energy and ore-forming potential of 600 °C mid-ocean-ridge hydrothermal fluids. *Geology*, *48*(12), 1221–1225. https://doi.org/10.1130/G47791.1

Ban, M., Hirotani, S., Wako, A., Suga, T., Iai, Y., Kagashima, S., et al. (2007). Origin of felsic magmas in a large-caldera-related stratovolcano in the central part of NE Japan — Petrogenesis of the Takamatsu volcano. *Journal of Volcanology and Geothermal Research*, *167*(1), 100–118. https://doi.org/10.1016/j.jvolgeores.2007.05.008

Bannard, J. E. (1975). Effect of density on the electrical conductance of aqueous sodium chloride solutions. *Journal of Applied Electrochemistry*, *5*(1), 43–53. https://doi.org/10.1007/BF00625958

Becken, M., Ritter, O., Bedrosian, P. A., & Weckmann, U. (2011). Correlation between deep fluids, tremor and creep along the central San Andreas fault. *Nature*, *480*(7375), 87–90. https://doi.org/10.1038/nature10609

Bedrosian, P. A., Peacock, J. R., Bowles-Martinez, E., Schultz, A., & Hill, G. J. (2018). Crustal inheritance and a top-down control on arc magmatism at Mount St Helens. *Nature Geoscience*, *11*(11), 865–870. https://doi.org/10.1038/s41561-018-0217-2

Bertrand, E. A., Caldwell, T. G., Hill, G. J., Wallin, E. L., Bennie, S. L., Cozens, N., et al. (2012). Magnetotelluric imaging of upper-crustal convection plumes beneath the Taupo Volcanic Zone, New Zealand. *Geophysical Research Letters*, *39*(2). https://doi.org/10.1029/2011GL050177

Blundy, J., Afanasyev, A., Tattitch, B., Sparks, S., Melnik, O., Utkin, I., & Rust, A. (2021). The economic potential of metalliferous sub-volcanic brines. *Royal Society Open Science*, *8*(6), 202192. https://doi.org/10.1098/rsos.202192

Bowles-Martinez, E., & Schultz, A. (2020). Composition of magma and characteristics of the hydrothermal system of Newberry volcano, Oregon, from Magnetotellurics. *Geochemistry, Geophysics, Geosystems*, *21*(3), e2019GC008831. https://doi.org/10.1029/2019GC008831

Caldwell, T. G., Bibby, H. M., & Brown, C. (2004). The magnetotelluric phase tensor. *Geophysical Journal International*, *158*(2), 457–469. https://doi.org/10.1111/j.1365-246X.2004.02281.x

599 Chave, A. D., & Jones, A. G. (2012). Introduction to the magnetotelluric method. In *The*
600 *Magnetotelluric Method: Theory and Practice* (p. 570). Cambridge: Cambridge University
601 Press. https://doi.org/10.1017/CBO9781139020138.002
602 Cherkose, B. A., & Saibi, H. (2021). Investigation of the Ayrobera geothermal field using 3D
603 magnetotelluric data inversion, Afar depression, NE Ethiopia. *Geothermics*, *94*, 102114.
604 https://doi.org/10.1016/j.geothermics.2021.102114
605 Comeau, M. J., Becken, M., Connolly, J. A. D., Grayver, A. V., & Kuvshinov, A. V. (2020).
606 Compaction‐driven fluid localization as an explanation for lower crustal electrical
607 conductors in an intracontinental setting. *Geophysical Research Letters*, *47*(19),
608 e2020GL088455. https://doi.org/10.1029/2020GL088455
609 Constable, S., Parker, R. L., & Constable, C. G. (1987). Occam's inversion: A practical algorithm
610 for generating smooth models from electromagnetic sounding data. *Geophysics*, *52*(3), 289–
611 300. https://doi.org/10.1190/1.1442303
612 Cordell, D., Unsworth, M. J., Lee, B., Díaz, D., Bennington, N. L., & Thurber, C. H. (2020).
613 Integrating magnetotelluric and seismic images of silicic magma systems: A case study from
614 the Laguna del Maule Volcanic Field, central Chile. *Journal of Geophysical Research: Solid*
615 *Earth*, *125*(11), e2020JB020459. https://doi.org/10.1029/2020JB020459
616 Di Paolo, F., Ledo, J., Ślęzak, K., Martínez van Dorth, D., Cabrera-Pérez, I., & Pérez, N. M.
617 (2020). La Palma island (Spain) geothermal system revealed by 3D magnetotelluric data
618 inversion. *Scientific Reports*, *10*(1), 18181. https://doi.org/10.1038/s41598-020-75001-z
619 Doi, N., Kato, O., Ikeuchi, K., Komatsu, R., Miyazaki, S., Akaku, K., & Uchida, T. (1998).
620 Genesis of the plutonic-hydrothermal system around quaternary granite in the kakkonda
621 geothermal system, Japan. *Geothermics*, *27*(5), 663–690. https://doi.org/10.1016/S0375-
622 6505(98)00039-X
623 Driesner, T., & Heinrich, C. A. (2007). The system H2O–NaCl. Part I: Correlation formulae for
624 phase relations in temperature–pressure–composition space from 0 to 1000°C, 0 to 5000bar,
625 and 0 to 1 XNaCl. *Geochimica et Cosmochimica Acta*, *71*(20), 4880–4901.
626 https://doi.org/10.1016/j.gca.2006.01.033
627 Elders, W. A., Friðleifsson, G. Ó., & Albertsson, A. (2014). Drilling into magma and the
628 implications of the Iceland Deep Drilling Project (IDDP) for high-temperature geothermal
629 systems worldwide. *Geothermics*, *49*, 111–118.
630 https://doi.org/10.1016/j.geothermics.2013.05.001
631 Farquharson, C. G. (2008). Constructing piecewise-constant models in multidimensional
632 minimum-structure inversions. *Geophysics*, *73*(1), K1–K9. https://doi.org/10.1190/1.2816650
633 Feucht, D. W., Sheehan, A. F., & Bedrosian, P. A. (2017). Magnetotelluric imaging of lower
634 crustal melt and lithospheric hydration in the Rocky Mountain Front transition zone, Colorado,
635 USA. *Journal of Geophysical Research: Solid Earth*, *122*(12), 9489–9510.
636 https://doi.org/10.1002/2017JB014474
637 Fournier, R. O. (1999). Hydrothermal processes related to movement of fluid from plastic into
638 brittle rock in the magmatic-epithermal environment. *Economic Geology*, *94*(8), 1193–1211.
639 https://doi.org/10.2113/gsecongeo.94.8.1193
640 Friðleifsson, G. Ó., Elders, W. A., Zierenberg, R. A., Fowler, A. P. G., Weisenberger, T. B.,
641 Mesfin, K. G., et al. (2020). The Iceland Deep Drilling Project at Reykjanes: Drilling into the
642 root zone of a black smoker analog. *Journal of Volcanology and Geothermal Research*, *391*,
643 106435. https://doi.org/10.1016/j.jvolgeores.2018.08.013
644 Gaillard, F., & Marziano, G. I. (2005). Electrical conductivity of magma in the course of

crystallization controlled by their residual liquid composition. *Journal of Geophysical Research: Solid Earth*, *110*(B6). https://doi.org/10.1029/2004JB003282

Gresse, M., Uyeshima, M., Koyama, T., Hase, H., Aizawa, K., Yamaya, Y., et al. (2021). Hydrothermal and magmatic system of a volcanic island inferred from magnetotellurics, seismicity, self-potential, and thermal image: an example of Miyakejima (Japan). *Journal of Geophysical Research: Solid Earth*, *126*(6), e2021JB022034. https://doi.org/10.1029/2021JB022034

Guo, X., Li, B., Ni, H., & Mao, Z. (2017). Electrical conductivity of hydrous andesitic melts pertinent to subduction zones. *Journal of Geophysical Research: Solid Earth*, *122*(3), 1777–1788. https://doi.org/10.1002/2016JB013524

Hasegawa, A., Zhao, D., Hori, S., Yamamoto, A., & Horiuchi, S. (1991). Deep structure of the northeastern Japan arc and its relationship to seismic and volcanic activity. *Nature*, *352*(6337), 683–689. https://doi.org/10.1038/352683a0

Hashin, Z., & Shtrikman, S. (1962). A variational approach to the theory of the effective magnetic permeability of multiphase materials. *Journal of Applied Physics*, *33*(10), 3125–3131. https://doi.org/10.1063/1.1728579

Hata, M., Oshiman, N., Yoshimura, R., Tanaka, Y., & Uyeshima, M. (2015). Three-dimensional electromagnetic imaging of upwelling fluids in the Kyushu subduction zone, Japan. *Journal of Geophysical Research: Solid Earth*, *120*(1), 1–17. https://doi.org/10.1002/2014JB011336

Heinrich, C. A. (2005). The physical and chemical evolution of low-salinity magmatic fluids at the porphyry to epithermal transition: a thermodynamic study. *Mineralium Deposita*, *39*(8), 864–889. https://doi.org/10.1007/s00126-004-0461-9

Heinson, G., Didana, Y., Soeffky, P., Thiel, S., & Wise, T. (2018). The crustal geophysical signature of a world-class magmatic mineral system. *Scientific Reports*, *8*(1), 10608. https://doi.org/10.1038/s41598-018-29016-2

Heise, W., Caldwell, T. G., Bibby, H. M., & Bannister, S. C. (2008). Three-dimensional modelling of magnetotelluric data from the Rotokawa geothermal field, Taupo Volcanic Zone, New Zealand. *Geophysical Journal International*, *173*(2), 740–750. https://doi.org/10.1111/j.1365-246X.2008.03737.x

Hill, G. J., Caldwell, T. G., Heise, W., Chertkoff, D. G., Bibby, H. M., Burgess, M. K., et al. (2009). Distribution of melt beneath Mount St Helens and Mount Adams inferred from magnetotelluric data. *Nature Geoscience*, *2*(11), 785–789. https://doi.org/10.1038/ngeo661

Horiguchi, K., Ueki, S., Sano, Y., Takahata, N., Hasegawa, A., & Igarashi, G. (2010). Geographical distribution of helium isotope ratios in northeastern Japan. *Island Arc*, *19*(1), 60–70. https://doi.org/10.1111/j.1440-1738.2009.00703.x

Hyndman, R. D., & Shearer, P. M. (1989). Water in the lower continental crust: modelling magnetotelluric and seismic reflection results. *Geophysical Journal International*, *98*(2), 343–365. https://doi.org/10.1111/j.1365-246X.1989.tb03357.x

Ichihara, H., Mogi, T., Tanimoto, K., Yamaya, Y., Hashimoto, T., Uyeshima, M., & Ogawa, Y. (2016). Crustal structure and fluid distribution beneath the southern part of the Hidaka collision zone revealed by 3-D electrical resistivity modeling. *Geochemistry, Geophysics, Geosystems*, *17*(4), 1480–1491. https://doi.org/10.1002/2015GC006222

Ichiki, M., Kaida, T., Nakayama, T., Miura, S., Yamamoto, M., Morita, Y., & Uyeshima, M. (2021). Magma reservoir beneath Azumayama Volcano, NE Japan, as inferred from a three-dimensional electrical resistivity model explored by means of magnetotelluric method. *Earth, Planets and Space*, *73*(1), 150. https://doi.org/10.1186/s40623-021-01451-y

691 Ikeuchi, K., Doi, N., Sakagawa, Y., Kamenosono, H., & Uchida, T. (1998). High-temperature
692 measurements in well WD-1A and the thermal structure of the kakkonda geothermal system,
693 Japan. *Geothermics*, *27*(5), 591–607. https://doi.org/10.1016/S0375-6505(98)00035-2
694 Ingebritsen, S. E., & Manning, C. E. (2010). Permeability of the continental crust: dynamic
695 variations inferred from seismicity and metamorphism. *Geofluids*, *10*(1-2), 193–205.
696 https://doi.org/10.1111/j.1468-8123.2010.00278.x
697 Ingham, M. R., Bibby, H. M., Heise, W., Jones, K. A., Cairns, P., Dravitzki, S., et al. (2009). A
698 magnetotelluric study of Mount Ruapehu volcano, New Zealand. *Geophysical Journal*
699 *International*, *179*(2), 887–904. https://doi.org/10.1111/j.1365-246X.2009.04317.x
700 Ishizu, K., Ogawa, Y., Mogi, T., Yamaya, Y., & Uchida, T. (2021). Ability of the magnetotelluric
701 method to image a deep conductor: Exploration of a supercritical geothermal system.
702 *Geothermics*, *96*, 102205. https://doi.org/10.1016/j.geothermics.2021.102205
703 Kanda, W., Utsugi, M., Takakura, S., & Inoue, H. (2019). Hydrothermal system of the active crater
704 of Aso volcano (Japan) inferred from a three-dimensional resistivity structure model. *Earth,*
705 *Planets and Space*, *71*(1), 37. https://doi.org/10.1186/s40623-019-1017-7
706 Kawamoto, T., Yoshikawa, M., Kumagai, Y., Mirabueno, M. H. T., Okuno, M., & Kobayashi, T.
707 (2013). Mantle wedge infiltrated with saline fluids from dehydration and decarbonation of
708 subducting slab. *Proceedings of the National Academy of Sciences of the United States of*
709 *America*, *110*(24), 9663–9668. https://doi.org/10.1073/pnas.1302040110
710 Kelbert, A., Meqbel, N., Egbert, G. D., & Tandon, K. (2014). ModEM: A modular system for
711 inversion of electromagnetic geophysical data. *Computers & Geosciences*, *66*, 40–53.
712 https://doi.org/10.1016/j.cageo.2014.01.010
713 Kita, I., Nagao, K., Nakamura, Y., & Taguchi, S. (1992). Information on geothermal system
714 obtained by chemical and isotropic charactics of soil and fumarolic gases from the Doroyu-
715 Kawarage geothermal field, Akita, Japan. *Journal of the Geothermal Research Society of*
716 *Japan*, *14*(2), 115–128 (in Japanese). https://doi.org/10.11367/grsj1979.14.115
717 Laumonier, M., Gaillard, F., & Sifre, D. (2015). The effect of pressure and water concentration on
718 the electrical conductivity of dacitic melts: Implication for magnetotelluric imaging in
719 subduction areas. *Chemical Geology*, *418*, 66–76.
720 https://doi.org/10.1016/j.chemgeo.2014.09.019
721 Le Pape, F., Jones, A. G., Unsworth, M. J., Vozar, J., Wei, W., Jin, S., et al. (2015). Constraints on
722 the evolution of crustal flow beneath Northern Tibet. *Geochemistry, Geophysics, Geosystems*,
723 *16*(12), 4237–4260. https://doi.org/10.1002/2015GC005828
724 Ledo, J., García-Merino, M., Larnier, H., Slezak, K., Piña-Varas, P., Marcuello, A., et al. (2021).
725 3D electrical resistivity of Gran Canaria island using magnetotelluric data. *Geothermics*, *89*,
726 101945. https://doi.org/10.1016/j.geothermics.2020.101945
727 Lee, B., Unsworth, M., Árnason, K., & Cordell, D. (2020). Imaging the magmatic system beneath
728 the Krafla geothermal field, Iceland: A new 3-D electrical resistivity model from inversion of
729 magnetotelluric data. *Geophysical Journal International*, *220*(1), 541–567.
730 https://doi.org/10.1093/gji/ggz427
731 Lowell, R. P., Van Cappellen, P., & Germanovich, L. N. (1993). Silica precipitation in fractures
732 and the evolution of permeability in hydrothermal upflow zones. *Science*, *260*(5105), 192.
733 https://doi.org/10.1126/science.260.5105.192
734 Manning, C. E. (1994). The solubility of quartz in H2O in the lower crust and upper mantle.
735 *Geochimica et Cosmochimica Acta*, *58*(22), 4831–4839. https://doi.org/10.1016/0016-
736 7037(94)90214-3

737 Mitsuhata, Y., Ogawa, Y., Mishina, M., Kono, T., Yokokura, T., & Uchida, T. (2001).
738 Electromagnetic heterogeneity of the seismogenic region of 1962 M6.5 Northern Miyagi
739 Earthquake, northeastern Japan. *Geophysical Research Letters*, *28*(23), 4371–4374.
740 https://doi.org/10.1029/2001GL013079
741 Monecke, T., Monecke, J., Reynolds, T. J., Tsuruoka, S., Bennett, M. M., Skewes, W. B., & Palin,
742 R. M. (2018). Quartz solubility in the H2O-NaCl system: A framework for understanding
743 vein formation in porphyry copper deposits. *Economic Geology*, *113*(5), 1007–1046.
744 https://doi.org/10.5382/econgeo.2018.4580
745 Moorkamp, M., Fishwick, S., Walker, R. J., & Jones, A. G. (2019). Geophysical evidence for
746 crustal and mantle weak zones controlling intra-plate seismicity – the 2017 Botswana
747 earthquake sequence. *Earth and Planetary Science Letters*, *506*, 175–183.
748 https://doi.org/10.1016/j.epsl.2018.10.048
749 Muraoka, H., Uchida, T., Sasada, M., Yagi, M., Akaku, K., Sasaki, M., et al. (1998). Deep
750 geothermal resources survey program: igneous, metamorphic and hydrothermal processes in a
751 well encountering 500°C at 3729 m depth, kakkonda, japan. *Geothermics*, *27*(5), 507–534.
752 https://doi.org/10.1016/S0375-6505(98)00031-5
753 Nakajima, J., Matsuzawa, T., Hasegawa, A., & Zhao, D. (2001). Seismic imaging of arc magma
754 and fluids under the central part of northeastern Japan. *Tectonophysics*, *341*(1), 1–17.
755 https://doi.org/10.1016/S0040-1951(01)00181-0
756 New Energy and Industrial Technology Development Organization. (1990). Final report on survey
757 to identify and promote geothermal development at Minase field, 1121 pp (in Japanese).
758 Retrieved from https://geothermal.jogmec.go.jp/report/nedo/file/30.pdf
759 Newman, G. A. (2014). A Review of High-Performance Computational Strategies for Modeling
760 and Imaging of Electromagnetic Induction Data. *Surveys in Geophysics*, *35*(1), 85–100.
761 https://doi.org/10.1007/s10712-013-9260-0
762 Nono, F., Gibert, B., Parat, F., Loggia, D., Cichy, S. B., & Violay, M. (2020). Electrical
763 conductivity of Icelandic deep geothermal reservoirs up to supercritical conditions: Insight
764 from laboratory experiments. *Journal of Volcanology and Geothermal Research*, *391*, 106364.
765 https://doi.org/10.1016/j.jvolgeores.2018.04.021
766 Nunohara, K., Okano, H., Yamada, R., Hirano, N., & Tsuchiya, N. (2021). Geothermal potentiality
767 in southern part of the Sanzugawa Caldera, Akita prefecture, Northeast Japan. *Journal of the*
768 *Geothermal Research Society of Japan*, *24*(4), 313–314 (in Japanese).
769 Ogawa, Y., & Uchida, T. (1996). A two-dimensional magnetotelluric inversion assuming Gaussian
770 static shift. *Geophysical Journal International*, *126*(1), 69–76. https://doi.org/10.1111/j.1365-
771 246X.1996.tb05267.x
772 Ogawa, Y., Mishina, M., Goto, T., Satoh, H., Oshiman, N., Kasaya, T., et al. (2001).
773 Magnetotelluric imaging of fluids in intraplate earthquake zones, NE Japan Back Arc.
774 *Geophysical Research Letters*, *28*(19), 3741–3744. https://doi.org/10.1029/2001GL013269
775 Ogawa, Y., Ichiki, M., Kanda, W., Mishina, M., & Asamori, K. (2014). Three-dimensional
776 magnetotelluric imaging of crustal fluids and seismicity around Naruko volcano, NE Japan.
777 *Earth, Planets and Space*, *66*(1), 158. https://doi.org/10.1186/s40623-014-0158-y
778 Okada, T., Matsuzawa, T., Nakajima, J., Uchida, N., Yamamoto, M., Hori, S., et al. (2014).
779 Seismic velocity structure in and around the Naruko volcano, NE Japan, and its implications
780 for volcanic and seismic activities. *Earth, Planets and Space*, *66*(1), 114.
781 https://doi.org/10.1186/1880-5981-66-114
782 Okamoto, K., Asanuma, H., Ishibashi, T., Yamaya, Y., Saishu, H., Yanagisawa, N., et al. (2019).

Geological and engineering features of developing ultra-high-temperature geothermal systems in the world. *Geothermics*, *82*, 267–281. https://doi.org/10.1016/j.geothermics.2019.07.002

Parisio, F., Vilarrasa, V., Wang, W., Kolditz, O., & Nagel, T. (2019). The risks of long-term re-injection in supercritical geothermal systems. *Nature Communications*, *10*(1), 4391. https://doi.org/10.1038/s41467-019-12146-0

Peacock, J. R., Mangan, M. T., McPhee, D., & Ponce, D. A. (2015). Imaging the magmatic system of Mono Basin, California, with magnetotellurics in three dimensions. *Journal of Geophysical Research: Solid Earth*, *120*(11), 7273–7289. https://doi.org/10.1002/2015JB012071

Peacock, J. R., Earney, T. E., Mangan, M. T., Schermerhorn, W. D., Glen, J. M., Walters, M., & Hartline, C. (2020). Geophysical characterization of the Northwest Geysers geothermal field, California. *Journal of Volcanology and Geothermal Research*, *399*, 106882. https://doi.org/10.1016/j.jvolgeores.2020.106882

Piana Agostinetti, N., Licciardi, A., Piccinini, D., Mazzarini, F., Musumeci, G., Saccorotti, G., & Chiarabba, C. (2017). Discovering geothermal supercritical fluids: a new frontier for seismic exploration. *Scientific Reports*, *7*(1), 14592. https://doi.org/10.1038/s41598-017-15118-w

Piña-Varas, P., Ledo, J., Queralt, P., Marcuello, A., & Perez, N. (2018). On the detectability of Teide volcano magma chambers (Tenerife, Canary Islands) with magnetotelluric data. *Earth, Planets and Space*, *70*(1), 14. https://doi.org/10.1186/s40623-018-0783-y

Pommier, A., & Le-Trong, E. (2011). "SIGMELTS": A web portal for electrical conductivity calculations in geosciences. *Computers & Geosciences*, *37*(9), 1450–1459. https://doi.org/10.1016/j.cageo.2011.01.002

Quist, A. S., & Marshall, W. L. (1968). Electrical conductances of aqueous sodium chloride solutions from 0 to 800. degree. and at pressures to 4000 bars. *The Journal of Physical Chemistry*, *72*(2), 684–703. https://doi.org/10.1021/j100848a050

Reinsch, T., Dobson, P., Asanuma, H., Huenges, E., Poletto, F., & Sanjuan, B. (2017). Utilizing supercritical geothermal systems: a review of past ventures and ongoing research activities. *Geothermal Energy*, *5*(1), 16. https://doi.org/10.1186/s40517-017-0075-y

Revil, A., Qi, Y., Ghorbani, A., Coperey, A., Ahmed, A. S., Finizola, A., & Ricci, T. (2019). Induced polarization of volcanic rocks. 3. Imaging clay cap properties in geothermal fields. *Geophysical Journal International*, *218*(2), 1398–1427. https://doi.org/10.1093/gji/ggz207

Richards, J. P. (2011). Magmatic to hydrothermal metal fluxes in convergent and collided margins. *Ore Geology Reviews*, *40*(1), 1–26. https://doi.org/10.1016/j.oregeorev.2011.05.006

Saishu, H., Okamoto, A., & Tsuchiya, N. (2014). The significance of silica precipitation on the formation of the permeable–impermeable boundary within Earth's crust. *Terra Nova*, *26*(4), 253–259. https://doi.org/10.1111/ter.12093

Sakuma, H., & Ichiki, M. (2016). Electrical conductivity of NaCl-H2O fluid in the crust. *Journal of Geophysical Research: Solid Earth*, *121*(2), 577–594. https://doi.org/10.1002/2015JB012219

Samrock, F., Grayver, A. V., Eysteinsson, H., & Saar, M. O. (2018). Magnetotelluric image of transcrustal magmatic system beneath the Tulu Moye geothermal prospect in the Ethiopian Rift. *Geophysical Research Letters*, *45*(23), 12,847–12,855. https://doi.org/10.1029/2018GL080333

Scholz, C. H. (2019). *The Mechanics of Earthquakes and Faulting* (3rd ed.). Cambridge: Cambridge University Press. https://doi.org/10.1017/9781316681473

Scott, S., Driesner, T., & Weis, P. (2015). Geologic controls on supercritical geothermal resources above magmatic intrusions. *Nature Communications*, *6*(1), 7837.

https://doi.org/10.1038/ncomms8837
Sibson, R. H. (2020). Preparation zones for large crustal earthquakes consequent on fault-valve action. *Earth, Planets and Space*, *72*(1), 31. https://doi.org/10.1186/s40623-020-01153-x
Sillitoe, R. H. (2010). Porphyry copper systems. *Economic Geology*, *105*(1), 3–41. https://doi.org/10.2113/gsecongeo.105.1.3
Sinmyo, R., & Keppler, H. (2016). Electrical conductivity of NaCl-bearing aqueous fluids to 600 °C and 1 GPa. *Contributions to Mineralogy and Petrology*, *172*(1), 4. https://doi.org/10.1007/s00410-016-1323-z
Siripunvaraporn, W., & Egbert, G. (2009). WSINV3DMT: Vertical magnetic field transfer function inversion and parallel implementation. *Physics of the Earth and Planetary Interiors*, *173*(3), 317–329. https://doi.org/10.1016/j.pepi.2009.01.013
Siripunvaraporn, W., Egbert, G., Lenbury, Y., & Uyeshima, M. (2005). Three-dimensional magnetotelluric inversion: data-space method. *Physics of the Earth and Planetary Interiors*, *150*(1–3), 3–14. https://doi.org/10.1016/j.pepi.2004.08.023
Stimac, J., Wilmarth, M., Mandeno, P. E., Dobson, P., & Winick, J. (2017). Review of exploitable supercritical geothermal resources to 5 km at Geysers-Clear Lake, Salton Sea, and Coso. *GRC Transactions*, *41*, 806–835. Retrieved from https://publications.mygeoenergynow.org/grc/1033767.pdf
Takeno, N. (2000). Thermal and geochemical structure of the Uenotai geothermal system, Japan. *Geothermics*, *29*(2), 257–277. https://doi.org/10.1016/S0375-6505(99)00062-0
Tamanyu, S., Fujiwara, S., Ishikawa, J., & Jingu, H. (1998). Fracture system related to geothermal reservoir based on core samples of slim holes. Example from the Uenotai geothermal field, northern Honshu, Japan. *Geothermics*, *27*(2), 143–166. https://doi.org/10.1016/S0375-6505(97)10012-8
Tamura, Y., Tatsumi, Y., Zhao, D., Kido, Y., & Shukuno, H. (2002). Hot fingers in the mantle wedge: new insights into magma genesis in subduction zones. *Earth and Planetary Science Letters*, *197*(1), 105–116. https://doi.org/10.1016/S0012-821X(02)00465-X
Tatsumi, Y., Takahashi, T., Hirahara, Y., Chang, Q., Miyazaki, T., Kimura, J.-I., et al. (2008). New insights into andesite genesis: the role of mantle-derived calc-alkalic and crust-derived tholeiitic melts in magma differentiation beneath Zao Volcano, NE Japan. *Journal of Petrology*, *49*(11), 1971–2008. https://doi.org/10.1093/petrology/egn055
Tatsumi, Y. (1989). Migration of fluid phases and genesis of basalt magmas in subduction zones. *Journal of Geophysical Research: Solid Earth*, *94*(B4), 4697–4707. https://doi.org/10.1029/JB094iB04p04697
Tseng, K. H., Ogawa, Y., Nurhasan, Tank, S. B., Ujihara, N., Honkura, Y., et al. (2020). Anatomy of active volcanic edifice at the Kusatsu–Shirane volcano, Japan, by magnetotellurics: hydrothermal implications for volcanic unrests. *Earth, Planets and Space*, *72*(1), 161. https://doi.org/10.1186/s40623-020-01283-2
Tsuchiya, N., & Hirano, N. (2007). Chemical reaction diversity of geofluids revealed by hydrothermal experiments under sub- and supercritical states. *Island Arc*, *16*(1), 6–15. https://doi.org/10.1111/j.1440-1738.2007.00554.x
Tsuchiya, N., Yamada, R., & Uno, M. (2016). Supercritical geothermal reservoir revealed by a granite–porphyry system. *Geothermics*, *63*, 182–194. https://doi.org/10.1016/j.geothermics.2015.12.011
Tuttle, O. F., & Bowen, N. L. (1958). Origin of granite in the light of experimental studies in the system NaAlSi3O8–KAlSi3O8–SiO2–H2O. In O. F. Tuttle & N. L. Bowen (Eds.), *Origin of*

Granite in the Light of Experimental Studies in the System NaAlSi3O8–KAlSi3O8–SiO2–H2O (Vol. 74, p. 0). Geological Society of America. https://doi.org/10.1130/MEM74-p1

Umeda, K., Hayashi, S., & Ban, M. (1999). K-Ar ages of Zarumori, Takamatsu, Funagata and Sankichi-Hayama volcanoes, NE Japan. *Bulletin of the Volcanological Society of Japan*, *44*(4), 217–222 (in Japanese). https://doi.org/10.18940/kazan.44.4_217

Unsworth, M. J., Jones, A. G., Wei, W., Marquis, G., Gokarn, S. G., Spratt, J. E., et al. (2005). Crustal rheology of the Himalaya and Southern Tibet inferred from magnetotelluric data. *Nature*, *438*(7064), 78–81. https://doi.org/10.1038/nature04154

Ussher, G., Harvey, C., Johnstone, R., & Anderson, E. (2000). Understanding the resistivities observed in geothermal systems. In *proceedings world geothermal congress* (pp. 1915–1920). Kyushu. Retrieved from https://www.geothermal-energy.org/pdf/IGAstandard/WGC/2000/R0279.PDF

Wallace, P. J. (2005). Volatiles in subduction zone magmas: concentrations and fluxes based on melt inclusion and volcanic gas data. *Journal of volcanology and Geothermal Research*, *140*(1), 217–240. https://doi.org/10.1016/j.jvolgeores.2004.07.023

Wannamaker, P. E., Caldwell, T. G., Jiracek, G. R., Maris, V., Hill, G. J., Ogawa, Y., et al. (2009). Fluid and deformation regime of an advancing subduction system at Marlborough, New Zealand. *Nature*, *460*(7256), 733–736. https://doi.org/10.1038/nature08204

Watanabe, N., Numakura, T., Sakaguchi, K., Saishu, H., Okamoto, A., Ingebritsen, S. E., & Tsuchiya, N. (2017). Potentially exploitable supercritical geothermal resources in the ductile crust. *Nature Geoscience*, *10*(2), 140–144. https://doi.org/10.1038/ngeo2879

Watanabe, T., & Peach, C. J. (2002). Electrical impedance measurement of plastically deforming halite rocks at 125°C and 50 MPa. *Journal of Geophysical Research: Solid Earth*, *107*(B1), ECV 2-1-ECV 2-12. https://doi.org/10.1029/2001JB000204

Weatherley, D., & Henley, R. (2013). Flash vaporization during earthquakes evidenced by gold deposits. *Nature Geoscience*, *6*, 294–298. https://doi.org/10.1038/ngeo1759

Weis, P., Driesner, T., & Heinrich, C. A. (2012). Porphyry-copper ore shells form at stable pressure-temperature fronts within dynamic fluid plumes. *Science*, *338*(6114), 1613. https://doi.org/10.1126/science.1225009

Wersin, P., Johnson, L. H., & McKinley, I. G. (2007). Performance of the bentonite barrier at temperatures beyond 100°C: A critical review. *Physics and Chemistry of the Earth*, *32*(8), 780–788. https://doi.org/10.1016/j.pce.2006.02.051

Wise, T., & Thiel, S. (2020). Proterozoic tectonothermal processes imaged with magnetotellurics and seismic reflection in southern Australia. *Geoscience Frontiers*, *11*(3), 885–893. https://doi.org/10.1016/j.gsf.2019.09.006

Yamaya, Y., Alanis, P. K. B., Takeuchi, A., Cordon, J. M., Mogi, T., Hashimoto, T., et al. (2013). A large hydrothermal reservoir beneath Taal Volcano (Philippines) revealed by magnetotelluric resistivity survey: 2D resistivity modeling. *Bulletin of Volcanology*, *75*(7), 729. https://doi.org/10.1007/s00445-013-0729-y

Yamaya, Y., Mogi, T., Honda, R., Hase, H., Hashimoto, T., & Uyeshima, M. (2017). Three-dimensional resistivity structure in Ishikari Lowland, Hokkaido, northeastern Japan—Implications to strain concentration mechanism. *Geochemistry, Geophysics, Geosystems*, *18*(2), 735–754. https://doi.org/10.1002/2016GC006771

Yoshida, T., Kimura, J.-I., Yamada, R., Acocella, V., Sato, H., Zhao, D., et al. (2014). Evolution of late Cenozoic magmatism and the crust–mantle structure in the NE Japan Arc. *Geological Society, London, Special Publications*, *385*(1), 335. https://doi.org/10.1144/SP385.15

Yoshimura, R., Ogawa, Y., Yukutake, Y., Kanda, W., Komori, S., Hase, H., et al. (2018). Resistivity characterisation of Hakone volcano, Central Japan, by three-dimensional magnetotelluric inversion. *Earth, Planets and Space*, *70*(1), 66. https://doi.org/10.1186/s40623-018-0848-y